forum acusticum 2026
8-12 September · Graz, Austria

IN SITU CHARACTERIZATION OF NON-PLANAR SOUND ABSORBERS USING PHYSICS-INFORMED NEURAL OPERATORS

Jonas M. Schmid[1], Johannes D. Schmid[1], Steffen Marburg[1]
[1] *Chair of Vibroacoustics of Vehicles and Machines, Technical University of Munich, Germany*

This paper is a revised version of the authors' submitted manuscript that was peer-reviewed by at least two anonymous reviewers.

Abstract

Accurate characterization of acoustic boundary properties is essential for reliable acoustic simulations, yet existing *in situ* methods remain limited by model assumptions, computational cost, and sensitivity to noise. In this work, a physics-informed neural operator framework is proposed for directly estimating the frequency-dependent acoustic surface admittance from near-field measurements of sound pressure and particle velocity. The proposed approach employs a deep operator network architecture to learn the underlying neural operator that maps measurement data, spatial coordinates, and excitation frequency to the corresponding acoustic field quantities, thereby enabling the simultaneous estimation of the complex-valued surface admittance spectrum. Notably, this formulation circumvents the need for an explicitly defined wave-propagation model or a computationally intensive numerical forward model. Physical consistency is ensured by embedding the governing acoustic relations, including the Helmholtz equation, the linearized momentum equation, and the Robin boundary condition, into the training process. The method is validated using synthetically generated data from a simulation model of a cylindrical absorber under semi free-field conditions. Results demonstrate accurate estimation of the complex-valued admittance over a wide frequency range from 250 to 5000 Hz. The proposed framework offers a neural network-based yet physically consistent alternative to conventional inverse methods, with particular advantages for the characterization of finite-sized and non-planar sound absorbers.

Keywords: *Physics-informed neural operator, surface admittance, surface impedance, in situ methods, physics-informed neural networks*

Corresponding author: *jonas.m.schmid@tum.de.*

1. Introduction

Wave-based acoustic simulation methods, most prominently the finite element method (FEM) and the boundary element method (BEM), have become indispensable in engineering acoustics. As emphasized by Vorländer [1], reliable predictions rely on an accurate description of the boundary properties of all acoustically interacting surfaces. In such models, boundary conditions are commonly expressed through the complex-valued surface impedance Z, or equivalently its reciprocal, the surface admittance Y [2]. The surface admittance is defined as the ratio of the normal component of the particle velocity to the acoustic sound pressure at the boundary $Y = v_n/p$ [2]. Because both amplitude and phase are encoded in these quantities, they are essential for physically accurate predictions.

Despite the growing prominence of wave-based approaches, comprehensive datasets of surface impedance remain scarce. This gap motivate the development of *in situ* measurement strategies that estimate acoustic boundary properties under realistic, application-relevant scenarios, without destructive specimen handling, specialized laboratory fixtures, or restrictive assumptions about the incident field. In contrast to the impedance-tube method, which enforces plane-wave propagation at normal incidence within a rigidly confined geometry, *in situ* techniques can accommodate oblique incidence, complex sound fields, and spatial heterogeneity, thereby yielding boundary characterizations that are more representative of real-world conditions [3].

A variety of *in situ* approaches have been proposed, most of which formulate boundary characterization as an inverse problem. These methods measure sound pressure and/or particle velocity in the near field of the specimen and subsequently infer surface quantities by solving an inverse problem based on physical models of wave propagation. The acoustic field is commonly expanded in elementary wave bases, e.g., plane waves [4], spherical waves [5] or complex image sources [6]. Measurements may be obtained sequentially by repositioning a single sensor or simultaneously using microphone arrays. As an alternative or complement, PU-probes acquire pressure and particle-velocity simultaneously in close proximity to the surface. The resulting data can be integrated with the aforementioned formulations to estimate boundary properties [7]. Estimating surface impedance from acoustic field data is an ill-posed inverse problem, inherently sensitive to noise and modeling inaccuracies. Regularization (e.g., Tikhonov regularization [4], sparsity-promoting approaches [5]), and Bayesian inference [8] are therefore widely employed to stabilize the solution.

In general, the fidelity and robustness of model-based inversions remain fundamentally constrained by the accuracy of the underlying wave propagation model [9]. Simplifying assumptions, such as infinite, locally reacting surfaces or idealized wave representations, can introduce systematic error. These are particularly pronounced at low frequencies where diffraction effects become significant [6] and for geometrically intricate objects [10]. Machine learning-based approaches have been proposed to compensate for these modeling inaccuracies [11], [12].

Discretization-based approaches employing FEM or BEM as forward models address some of these limitations by capturing complex geometries and wave phenomena more accurately. However, they are computationally demanding and typically require frequency-wise inversion [8], [10]. A recent approach by Schmid et al. [13] utilizing simulation-based inference offers a probabilistic framework for parameter estimation, yet it still depends on an accurate forward model and remains sensitive to model–data mismatch.

Physics-informed neural networks (PINNs) have emerged as a promising alternative by embedding governing equations directly into the learning process, enabling physically consistent predictions from sparse or noisy data [14]. Applications in acoustics include sound field prediction, reconstruction, and boundary parameter estimation [15]. However, PINNs are inherently limited to solving a single parameter instance, requiring retraining for each frequency, which restricts their applicability to frequency-dependent problems. Recently, Xia et al. [16] have proposed a physics-informed neural field method that infers impedance from pressure gradients frequency-wise using sparse pressure data, eliminating particle velocity measurements but increasing noise sensitivity and reducing low-frequency accuracy due to gradient errors.

Neural operators overcome this limitation by learning mappings between function spaces, allowing efficient prediction of solution fields across varying input parameters such as frequency [17]. They have recently been applied to a range of problems in acoustics and structural dynamics, including sound field prediction[18] and structural intensity estimation [19].

In this work, a physics-informed neural operator framework is proposed to directly estimate frequency-dependent acoustic surface admittance from near-field measurements of sound pressure and normal particle velocity. By incorporating frequency as an input variable, the method learns the full admittance spectrum within a single model, eliminating the need for frequency-wise inversion. At the same time, it avoids explicit analytical or numerical forward models by learning the mapping from measurements to field quantities and boundary parameters directly. The governing acoustic equations are inherently embedded into the training process, providing physics-based regularization. This yields computationally efficient, physically consistent, and spatially coherent admittance estimates, offering a promising alternative to conventional inverse approaches.

2. Model description

Simulated measurement data are generated using a BEM model of a non-planar sound absorber under semi free-field conditions. The considered geometry consists of a cylinder with diameter $D = 15\,\mathrm{cm}$ and height $h = 100\,\mathrm{cm}$, aligned with the z-axis, as illustrated in Fig. 1. The acoustic domain is modeled as

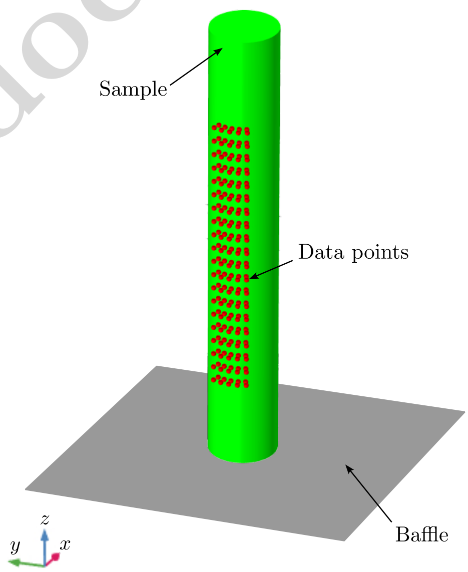

Figure 1: Geometrical model of the cylindrical sample under investigation (green) as well as the data points depicted in as red dots.

a half-space bounded by a rigid reflecting plane at $z = 0$. Acoustic excitation is provided by a monopole source located at $\mathbf{x}_S = (-2.0,\, 0.0,\, 0.5)\,\mathrm{m}$ with a pressure amplitude of $1\,\mathrm{Pa}$. The surrounding medium is air, characterized by a density $\rho_0 = 1.2\,\mathrm{kg\,m^{-3}}$ and a speed of sound $c = 343\,\mathrm{m\,s^{-1}}$, resulting in a characteristic impedance $Z_0 = \rho_0 c$. A spatially uniform, complex-valued surface admittance $\widetilde{Y}_{\mathrm{ref}}$ is prescribed on the cylinder boundary and expressed in dimensionless form as $Y_{\mathrm{ref}} = \widetilde{Y}_{\mathrm{ref}} Z_0$. The frequency-dependent reference admittance is derived from impedance tube measurements of a melamine foam sample with thickness $t = 35\,\mathrm{mm}$ and diameter $d = 40\,\mathrm{mm}$, conducted in accordance with ISO 10534-2. This admittance serves as a realistic frequency-dependent target spectrum for the synthetic study rather than a physically accurate representation of a permeable free-standing cylinder of the same material. The corresponding reference admittance spectrum is shown in gray color in Fig. 3. All simulations are performed using COMSOL Multiphysics.

The training data consist of collocated samples of the real- and imaginary parts of the acoustic pressure p and the normal particle velocity v_n, obtained at two radial layers in front of the cylinder. In practical applications, such measurements can be acquired using a PU-probe. The observation domain spans a $45°$ circumferential sector and remains within 10 cm from the bottom and top of the cylinder. A total of $N_D = 200$ measurement points are distributed within this region, as indicated by the red markers in Fig. 1. The inner measurement layer is located at a radial distance of 0.5 cm from the surface, while the outer layer is positioned 1.5 cm further outward. The sampling locations are arranged on a structured cylindrical grid of 20×5 points per layer. To emulate realistic measurement conditions, zero-mean Gaussian noise is added to both p and v_n, corresponding to a signal-to-noise ratio (SNR) of $\mathrm{SNR} = 40\,\mathrm{dB}$. The frequency range extends from 250 to 5000 Hz, with discrete frequencies selected at the center frequencies of the 1/12-octave bands.

3. Physics-informed neural operators

Neural operators approximate mappings between function spaces and are therefore well suited for parameterized PDE problems. In the present case, the underlying nonlinear solution operator maps the frequency input f to the corresponding complex-valued acoustic field quantities sound pressure $p(\mathbf{r})$ and the normal particle velocity $v_n(\mathbf{r})$ at spatial position $\mathbf{r} = [r, \phi, z]^T \in \Omega$ in cylindrical coordinates. This operator is approximated by a parameterized surrogate $\mathcal{G}_\theta$, which is trained from measurement data while simultaneously being constrained by the governing acoustic physics.

The operator is represented by a deep operator network (DeepONet) architecture consisting of a branch and a trunk network [17]. The branch network encodes the frequency input into a latent representation, whereas the trunk network maps the spatial coordinates to a spatial feature representation. Both latent vectors are combined through an inner product, such that the network predicts the acoustic quantities as a function of both frequency and position. This decomposition separates the frequency dependence from the spatial dependence and enables the trained model to evaluate the field at arbitrary spatial locations within the domain [20]. In practice, this generalization capability is contingent on an adequate sampling of the underlying function spaces. Here, the model is trained on samples of the complex-valued pressure and normal particle velocity acquired at discrete frequencies and spatial locations, which constitutes a discrete sampling of the frequency and spatial domains, respectively. In addition to supervised data fitting, physical consistency is enforced by augmenting the loss function with residuals of the governing equations [21]. The total objective is formulated as a weighted sum of two data losses and three physics-informed losses, namely

$$\mathcal{L}(\theta) = \lambda_p \mathcal{L}_p + \lambda_{v_n} \mathcal{L}_{v_n} + \lambda_{\mathrm{LM}} \mathcal{L}_{\mathrm{LM}} + \lambda_{\mathrm{Helm}} \mathcal{L}_{\mathrm{Helm}} + \lambda_{\mathrm{R}} \mathcal{L}_{\mathrm{R}}.$$

Here, $\mathcal{L}_p$ and $\mathcal{L}_{v_n}$ are mean squared errors (MSE) between predicted and measured pressure and normal particle velocity at the measurement points, respectively. The remaining terms impose the linearized momentum equation, the Helmholtz equation, and the Robin boundary condition as detailed subsequently. The weighting coefficients control the relative contributions of the individual loss terms to the total loss $\mathcal{L}(\theta)$.

The loss term $\mathcal{L}_{\mathrm{LM}}$ enforces the linearized momentum equation in frequency domain

$$\frac{\partial p}{\partial r} = -i\omega\rho_0 v_n, \tag{1}$$

where $\omega = 2\pi f$ denotes the angular frequency. It relates the pressure gradient in radial (normal) direction to the normal particle velocity. This residual is evaluated at the measurement locations and uses the measured velocity to constrain the predicted pressure gradient. In this way, the data not only supervise the field values directly, but also constrain their physically consistent differential relation. This improves the coupling between pressure and velocity predictions and stabilizes training.

The loss term $\mathcal{L}_{\mathrm{Helm}}$ enforces the governing Helmholtz equation in the acoustic domain. Rather than using the Helmholtz equation in its original form, a mixed formulation is adopted in which the pressure derivative in normal direction is replaced using the momentum equation in Eq. (1). Substitution into the cylindrical Helmholtz equation yields

$$-i\omega\rho_0 \frac{\partial v_n}{\partial r} - \frac{i\omega\rho_0}{r} v_n + \frac{1}{r^2}\frac{\partial^2 p}{\partial \phi^2} + \frac{\partial^2 p}{\partial z^2} + k^2 p = 0, \tag{2}$$

where $k = \omega / c_0$ is the acoustic wavenumber. This reformulation is advantageous because it lowers the derivative order that must be computed with respect to the network outputs in radial direction. Since higher-order derivatives obtained by automatic differentiation are known to be numerically delicate, this mixed form improves training robustness and reduces the risk of unstable gradients. The Helmholtz residual is evaluated at randomly sampled interior collocation points distributed across the acoustic domain between the sample surface and the outer measurement surface. Because this loss depends only on network predictions, it acts as a self-consistency constraint that regularizes the reconstructed field even in regions without direct measurements.

The boundary loss term $\mathcal{L}_R$ enforces the locally reacting Robin boundary condition at the sample surface at $r = R$ and is central for surface admittance identification. For a surface with spatially uniform normalized admittance Y, together with substituting the momentum equation Eq. (1) using the outward normal of the fluid domain, the boundary condition reads

$$i\omega\rho_0 v_n + ikYp = 0 \qquad \text{on } \Gamma_Y. \tag{3}$$

This residual is evaluated at boundary collocation points on the absorber surface. Importantly, the surface admittance Y is not computed in a separate post-processing step, but treated as an additional trainable quantity and optimized jointly with the network parameters. As a result, the admittance is inferred as the value that globally minimizes the boundary residual while remaining consistent with the measured data and the governing physics.

4. DeepONet architecture and training

The DeepONet architecture is realized using residual multilayer perceptrons equipped with sinusoidal activation functions in accordance with the SIREN formulation, which has proven particularly effective for representing oscillatory wave phenomena. To enhance numerical stability during training, frequency-wise normalization is applied to the real and imaginary components of both pressure and normal particle velocity, spatial coordinates are mapped onto a fixed interval, and the frequency input is appropriately transformed and standardized. In addition, the physics-based residual terms are scaled to ensure a frequency-balanced contribution of all loss components. The network hyperparameters, including the loss weighting factors as well as the network width and depth, are selected via a grid search comprising 50 configurations, each evaluated on the validation loss. This yields optimal weighting factors of $\lambda_p = 0.16$, $\lambda_{v_n} = 0.5$, $\lambda_{\mathrm{LM}} = 5.5 \times 10^{-3}$, $\lambda_{\mathrm{Helm}} = 6.8 \times 10^{-8}$, and $\lambda_{\mathrm{R}} = 1.5$. The synthetically generated dataset is divided into 90% for training and 10% for validation. Loss optimization is performed using the AdamW algorithm in conjunction with a cosine-annealing learning rate schedule. The overall computational effort amounts to approximately 35 min of wall-clock time for 50,000 training epochs on an NVIDIA GeForce RTX 5080 GPU.

Fig. 2 shows the evolution of the weighted training and validation losses during DeepONet training. The supervised data terms for pressure p and normal particle velocity v_n converge rapidly and smoothly, indicating effective learning of the measurement data. The physics-informed residual terms are then progressively activated through cosine ramps that increase their weighting factors from zero to their target values, causing a temporary rise followed by a consistent decay as the model adapts to the added constraints. The Helmholtz and Robin losses, in particular, peak transiently upon activation before stabilizing at lower magnitudes. This coupling is partly structural: the mixed Helmholtz formulation substitutes the linearized momentum equation in Eq. (1) and thus shares field quantities, while the Robin term, acting solely at the boundary $r = R$, selects the interior solution compatible with the prescribed surface admittance. Overall, the model integrates data-driven learning with physics-based regularization, converging across all loss components.

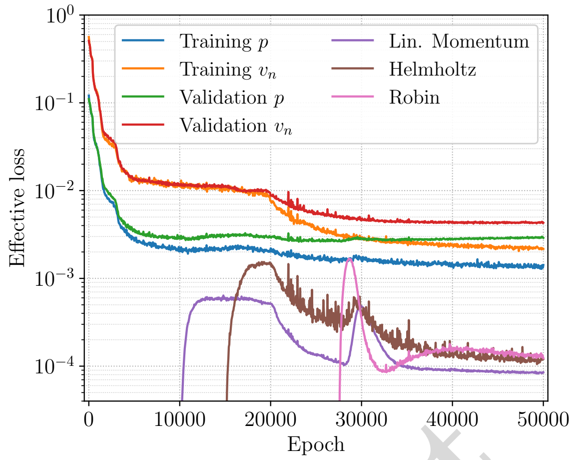

Figure 2: Evolution of the effective training and validation losses ($\lambda \cdot$ loss) throughout the DeepONet training process.

5. Results and discussion

Fig. 3 compares the real and imaginary parts of the acoustic surface admittance Y inferred by the DeepONet model with the reference spectrum over the frequency range from 250 to 5000 Hz. Note that Y is inferred as a global trainable parameter for a single physical configuration rather than the generalization of a forward map across unseen configurations.

Overall, the model accurately reproduces the frequency-dependent behavior of both components, including the pronounced peak in the real part around 2.2 kHz and the corresponding variation in the imaginary part, indicating a reliable reconstruction of the underlying boundary characteristics.

To quantitatively assess the reconstruction accuracy, the relative L_2-norm error is defined as

$$L_2 = \frac{\sqrt{\sum_{j=1}^{N} \left| Y_j^{\mathrm{pred}} - Y_j^{\mathrm{ref}} \right|^2}}{\sqrt{\sum_{j=1}^{N} \left| Y_j^{\mathrm{ref}} \right|^2}}, \tag{4}$$

where Y^{pred} and Y^{ref} denote the predicted and reference complex-valued surface admittances, respectively.

The frequency-dependent relative L_2-error is shown in Fig. 4. A clear minimum is observed in the mid-frequency range, where the reconstruction accuracy is

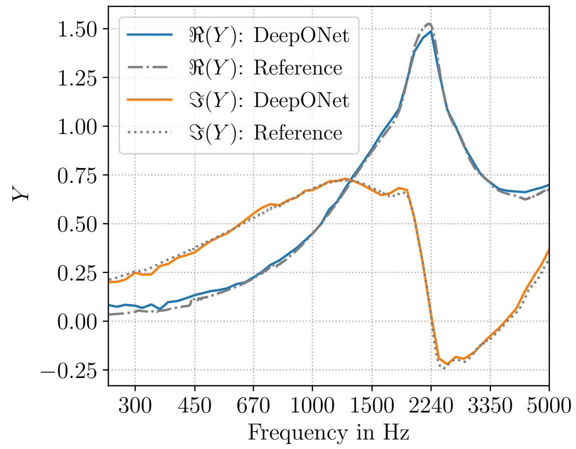

Figure 3: Comparison of the real and imaginary parts of the acoustic surface admittance Y predicted by the DeepONet model and the reference spectrum (gray), obtained from impedance-tube measurements as described in Sec. 2.

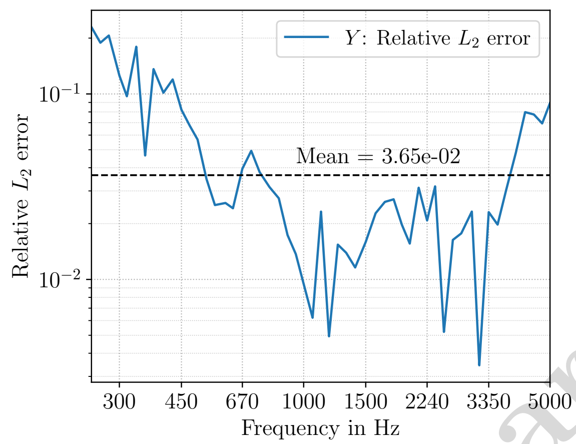

Figure 4: Relative L_2-error of the estimated acoustic surface admittance Y as a function of frequency. The dashed line indicates the mean error over the considered frequency range from 250 to 5000 Hz.

highest. This behavior is governed by the relationship between the acoustic wavelength λ and the characteristic cylinder diameter D. In this regime, where λ is comparable with the specimen dimensions, the acoustic field exhibits sufficiently rich spatial structure to encode the boundary admittance, while remaining well-resolved by the measurement configuration. As a result, both the sensitivity of the measurements to the boundary condition and the conditioning of the inverse problem are favorable.

At low frequencies, where $\lambda \gg D$, the cylinder behaves as an acoustically small object. The resulting scattered field exhibits predominantly monopole-like behavior, and admittance-induced perturbations in pressure and particle velocity are weak. In addition, the absorption of the sample is typically low in this regime, further reducing the influence of the boundary condition on the acoustic field. Consequently, spatial gradients are small and the measurements carry limited information about the boundary condition, leading to a poorly conditioned inverse problem. Moreover, the finite extent of the cylinder introduces deviations from idealized surface assumptions, further reducing identifiability.

At high frequencies, where $\lambda \ll D$, the acoustic field exhibits increasingly complex spatial variations and localized scattering effects. While this enhances the theoretical sensitivity to boundary properties, it also increases susceptibility to measurement noise, spatial undersampling, and model approximation errors. Furthermore, the finite size of the cylinder gives rise to pronounced diffraction and interference effects once multiple wavelengths fit across the structure, introducing additional wave phenomena that are difficult to capture and invert robustly.

Despite these frequency-dependent variations, the method achieves a low mean relative L_2-error of 3.65×10^{-2} over the entire frequency range from 250 to 5000 Hz, demonstrating its capability to accurately reconstruct complex, frequency-dependent boundary properties from sparse and noisy measurement data.

6. Conclusions

This work presents a neural-operator-based framework for the *in situ* estimation of acoustic boundary properties from near-field measurements of sound pressure and normal-direction particle velocity. In contrast to conventional approaches relying on explicit wave-propagation models or iterative inverse formulations, the method directly learns the mapping from acoustic field observations to frequency-dependent boundary quantities, with physical consistency ensured by embedding the Helmholtz equation, the linearized momentum equation, and the Robin boundary condition into the training process. The surface admittance is inferred as a global parameter, yielding spatially coherent and noise-robust estimates. Validated on synthetically generated data for a cylindrical absorber, the framework accurately reconstructs a spatially uniform admittance spectrum from 250 to 5000 Hz, including acoustically small and non-planar configurations, achieving a low mean relative L_2-error of 3.65×10^{-2}. This accuracy is, however, established for a single fixed test configuration: the present study does not address generalization to different source positions, additional reflecting surfaces, or altered cylinder diameters, as the operator is trained for one measurement setup. The method thus represents an accurate and physically consistent alternative to conventional measurement approaches, at the cost of requiring comparatively large amounts of high-quality measurement data and careful hyperparameter tuning.

Future work will incorporate the source position and specimen geometry as additional operator inputs, enabling generalization across configurations without retraining, and will explore transfer learning to efficiently adapt the trained model to different acoustic surroundings. Further efforts will focus on experimental validation under realistic conditions, on benchmarking against established PU-based techniques such as cylindrical near-field acoustical holography, and on extending the approach toward the non-invasive, data-driven characterization of acoustic materials.

7. Acknowledgments

This work has received funding from the European Union's Horizon Europe research and innovation program under the project "MELCHIOR", grant agreement No. 101073899.

References

[1] M. Vorländer, "Computer simulations in room acoustics: Concepts and uncertainties," *J. Acoust. Soc. Am.*, vol. 133, no. 3, pp. 1203–1213, 2013.

[2] S. Marburg and B. Nolte, *Computational Acoustics of Noise Propagation in Fluids - Finite and Boundary Element Methods*. Berlin: Springer-Verlag, 2008.

[3] E. Brandão, A. Lenzi, and S. Paul, "A review of the in situ impedance and sound absorption measurement techniques," *Acta Acustica united with Acustica*, vol. 101, no. 3, pp. 443–463, 2015.

[4] M. Nolan, "Estimation of angle-dependent absorption coefficients from spatially distributed in situ measurements," *J. Acoust. Soc. Am.*, vol. 147, no. 2, pp. 119–124, 2020.

[5] A. Richard, E. Fernandez-Grande, J. Brunskog, and C.-H. Jeong, "Estimation of surface impedance at oblique incidence based on sparse array processing," *J. Acoust. Soc. Am.*, vol. 141, no. 6, pp. 4115–4125, 2017.

[6] E. Brandão, W. D. Fonseca, P. H. Mareze, *et al.*, "Sound absorption estimation using the discrete complex image source method and array processing," *Mech. Syst. Signal Process.*, vol. 231, p. 112 617, 2025.

[7] Briere de la Hosseraye, Baltazar, M. Hornikx, and J. Yang, "In situ acoustic characterization of a locally reacting porous material by means of pu measurement and model fitting," *Applied Acoustics*, vol. 191, p. 108 669, 2022.

[8] J. M. Schmid, M. Eser, and S. Marburg, "Bayesian approach for the in situ estimation of the acoustic boundary admittance," *J. Theor. Comput. Acoust.*, vol. 31, no. 04, 2023.

[9] M. Eser, S. Mannhardt, C. Gurbuz, E. Brandão, and S. Marburg, "Free-field characterization of locally reacting sound absorbers using bayesian inference with sequential frequency transfer," *Mech. Syst. Signal Process.*, vol. 205, p. 110 780, 2023.

[10] Z.-W. Luo, C.-J. Zheng, Y.-B. Zhang, and C.-X. Bi, "Estimating the acoustical properties of locally reactive finite materials using the boundary element method," *J. Acoust. Soc. Am.*, vol. 147, no. 6, pp. 3917–3931, 2020.

[11] M. Müller-Giebeler, M. Berzborn, and M. Vorländer, "Free-field method for inverse characterization of finite porous acoustic materials using feed forward neural networks," *J. Acoust. Soc. Am.*, vol. 155, no. 6, pp. 3900–3914, 2024.

[12] L. Emmerich, P. Aste, E. Brandão, *et al.*, "A data-driven two-microphone method for in situ sound absorption measurements of porous materials," *J. Acoust. Soc. Am.*, vol. 158, no. 3, pp. 1711–1722, 2025.

[13] J. M. Schmid, J. D. Schmid, M. Eser, and S. Marburg, "In situ estimation of the acoustic surface impedance using simulation-based inference," *J. Acoust. Soc. Am.*, vol. 159, no. 1, pp. 422–436, 2026.

[14] M. Raissi, P. Perdikaris, and G. E. Karniadakis, "Physics-informed neural networks: A deep learning framework for solving forward and inverse problems involving nonlinear partial differential equations," *Journal of Computational Physics*, vol. 378, pp. 686–707, 2019.

[15] J. D. Schmid, P. Bauerschmidt, C. Gurbuz, M. Eser, and S. Marburg, "Physics-informed neural networks for acoustic boundary admittance estimation," *Mech. Syst. Signal Process.*, vol. 215, p. 111 405, 2024.

[16] Y. Xia, X. Li, M. Calafà, A. P. Engsig-Karup, and C.-H. Jeong, "Surface impedance inference via neural fields and sparse acoustic data obtained by a compact array," *ArXiv*, no. 2602.11425, 2026.

[17] L. Lu, P. Jin, G. Pang, Z. Zhang, and G. E. Karniadakis, "Learning nonlinear operators via deeponet based on the universal approximation theorem of operators," *Nature Machine Intelligence*, vol. 3, no. 3, pp. 218–229, 2021.

[18] N. Borrel-Jensen, S. Goswami, A. P. Engsig-Karup, G. E. Karniadakis, and C.-H. Jeong, "Sound propagation in realistic interactive 3d scenes with parameterized sources using deep neural operators," *Proc. Natl. Acad. Sci. U.S.A.*, vol. 121, no. 2, e2312159120, 2024.

[19] J. D. Schmid, S. F. Zettel, and S. Marburg, "Physics-informed neural operators for predicting structural intensity from laser doppler vibrometry measurements of plates," *Mech. Syst. Signal Process.*, vol. 248, p. 114 013, 2026.

[20] K. Azizzadenesheli, N. Kovachki, Z. Li, M. Liu-Schiaffini, J. Kossaifi, and A. Anandkumar, "Neural operators for accelerating scientific simulations and design," *Nature Reviews Physics*, vol. 6, no. 5, pp. 320–328, 2024.

[21] Z. Li, H. Zheng, N. Kovachki, *et al.*, "Physics-informed neural operator for learning partial differential equations," *ACM / IMS Journal of Data Science*, vol. 1, no. 3, pp. 1–27, 2024.